ARTICLE Open Access

Metal-induced n^+/n homojunction for ultrahigh electron mobility transistors

Ji-Min Park[1], Hyoung-Do Kim[1], Hongrae Joh[2], Seong Cheol Jang[1], Kyung Park[3], Yun Chang Park[4], Ho-Hyun Nahm[5], Yong-Hyun Kim[5], Sanghun Jeon[2] and Hyun-Suk Kim[1]

Abstract

A self-organized n^+/n homojunction is proposed to achieve ultrahigh performance of thin film transistors (TFTs) based on an amorphous (Zn,Ba)SnO_3 (ZBTO) semiconductor with sufficiently limited scattering centers. A deposited Al layer can induce a highly O-deficient (n^+) interface layer in the back channel of a-ZBTO without damaging the front channel layer via the formation of a metal-oxide interlayer between the metal and back channel. The n^+ layer can significantly improve the field-effect mobility by providing a relatively high concentration of free electrons in the front n-channel ZBTO, where the scattering of carriers is already controlled. In comparison with a Ti layer, the Al metal layer is superior, as confirmed by first-principles density functional theory (DFT) calculations, due to the stronger metal-O bonds, which make it easier to form a metal oxide AlO_x interlayer through the removal of oxygen from ZBTO. The field-effect mobility of a-ZBTO with an Al capping layer can reach 153.4 cm^2/Vs, which is higher than that of the pristine device, i.e., 20.8 cm^2/Vs. This result paves the way for the realization of a cost-effective method for implementing indium-free ZBTO devices in various applications, such as flat panel displays and large-area electronic circuits.

Introduction

Thin-film transistors (TFTs) with amorphous oxide semiconductors (AOSs) have been incorporated into various display applications owing to their many advantages, such as their relatively high mobility (≥10 cm^2/Vs), large-area uniformity, and low-temperature process capability[1–3]. However, next-generation displays, such as 8 K (8000 × 4000) active-matrix organic light-emitting diode (AM-OLED) displays, demand much higher device performance capabilities, which will allow the integration of gate driver circuitry into these display panels. Typically, a field-effect mobility value of 50 cm^2/Vs or greater is required[4,5].

A number of high-mobility semiconductor materials, such as InZnO (IZO), InSnZnO (ITZO), ZnSnO (ZTO), and ZnON, have been reported in the literature[6–15]. Moreover, to further improve their device performance capabilities, structural modifications involving the use of dual gates or metal-capping approaches have been introduced[16–20]. In particular, metal-capping layers deposited between the source and drain electrodes have recently been reported to be effective in enhancing the field-effect mobility while preserving other electrical parameters[19,21]. Three main mechanisms are believed to be involved. The first is the scavenging effect of the scattering/trapping centers due to the metal layer, implying that the field-effect mobility of the AOSs should be improved due to the reduced scattering[18,19,21]. This can be easily understood because oxygen-related defects, such as weakly bonded or interstitial oxygen in the active channel layer, are preferentially removed during the formation of a metal-oxide layer[19,21]. The second mechanism is the metal-induced crystallization (MIC) of the active channel layer at low temperatures, which improves the transport of carriers by reducing the number of disorder defects in the channel material[19,22]. This is also

Correspondence: Ho-Hyun Nahm (hohyunnahm@kaist.ac.kr) or Sanghun Jeon (jeonsh@kaist.ac.kr) or Hyun-Suk Kim (khs3297@cnu.ac.kr)
[1]Department of Materials Science and Engineering, Chungnam National University, Daejeon 34134, Republic of Korea
[2]School of Electrical Engineering, Korea Advanced Institute of Science and Technology (KAIST), 291, Daehak-ro, Yuseong-gu, Daejeon, Republic of Korea
Full list of author information is available at the end of the article

© The Author(s) 2020

Open Access This article is licensed under a Creative Commons Attribution 4.0 International License, which permits use, sharing, adaptation, distribution and reproduction in any medium or format, as long as you give appropriate credit to the original author(s) and the source, provide a link to the Creative Commons license, and indicate if changes were made. The images or other third party material in this article are included in the article's Creative Commons license, unless indicated otherwise in a credit line to the material. If material is not included in the article's Creative Commons license and your intended use is not permitted by statutory regulation or exceeds the permitted use, you will need to obtain permission directly from the copyright holder. To view a copy of this license, visit http://creativecommons.org/licenses/by/4.0/.

understandable because the metal layer acts as a catalyst, easily breaking and rearranging the weakened metal-oxygen bonds in the channel during the postannealing process after the deposition of the metal layer. This phenomenon is referred to as the low-temperature MIC of the active layer. The final mechanism stems from an increase in the carrier concentration via electron injection from the metal into the active channel layer driven by the work function difference[20,23]. Based on band transport percolation or mobility edge models[24–26], the increased mobility can easily be supported. However, despite much effort in this area, it has been difficult to stably implement TFTs based on an ultrahigh-mobility amorphous oxide semiconductor with a field-effect mobility value exceeding 100 cm^2/Vs.

Fortunately, researchers have recently reported the theoretical design and experimental implementation of an amorphous (Zn,Ba)SnO_3 (a-ZBTO) semiconducting oxide, resulting in high-performance devices with excellent stability[27]. a-ZBTO tends to exhibit decreases in O-deficient states and band tail states as the $BaSnO_3$ (BTO) fraction increases, meaning that it can only achieve moderately high mobility due to the significantly reduced carrier concentration while maintaining the ultrahigh stability of TFTs. Hence, an ultrahigh field-effect mobility based on a-ZBTO can be expected if the free carrier concentration of a-ZBTO can be increased without compromising the (especially ultrastability-related) existing properties of a-ZBTO. For this reason, it is evident that a reliable strategy is to use a metal-capping approach on the a-ZBTO channel without a postannealing step to increase the carrier concentration without damaging the stability.

In this paper, we propose ultrahigh-mobility a-ZBTO-based TFTs achieved via the formation of an n^+/n homojunction induced by a metal-capping layer considering the collaborative outcomes of experiments and DFT calculations. The n^+/n homojunction can be self-organized through the formation of a highly O-deficient (n^+) interface layer in the back channel layer induced by a metal-oxide interlayer even without postannealing, providing a significant increase in the free carrier concentration for the front channel. Most electrons injected from the n^+ layer can be transported without serious scattering due to the low defect density of a-ZBTO. As a result, a device with an Al metal layer exhibits a remarkable field-effect mobility enhancement from 20.8 cm^2/Vs to 153.4 cm^2/Vs without significant degradation of other transfer parameters. TFTs with other active materials, in this case IZO and ZTO, were also examined for comparison. The mobility improvement of metal-capped ZBTO devices was far superior to those of IZO and ZTO TFTs. Additionally, to understand the major carrier transport mechanisms, we performed 1/f noise measurements on the ZBTO and Al-assisted ZBTO TFTs. Our results indicate that selecting a semiconducting channel material with few scattering centers, such as ZBTO, is a key factor during the fabrication of metal-assisted TFTs capable of ultrahigh performance.

Materials and methods

Device fabrication

ZBTO devices were fabricated on heavily doped p-type Si substrates with a thermally grown 100-nm-thick SiO_x dielectric material. Next, 20-nm-thick ZBTO active layers were deposited by cosputtering $ZnSnO_3$ and $BaSnO_3$ targets with RF powers of 80 and 10 W applied to the $ZnSnO_3$ and $BaSnO_3$ targets, respectively. The working pressure was 3 mTorr, while the Ar gas flow rate was fixed at 10 sccm. After depositing the active layer, thermal annealing was conducted at 350 °C for 1 h in air. Next, source-drain electrodes were formed by depositing a 150-nm-thick aluminum (Al) film by thermal evaporation using a shadow mask. The resulting channel width (W) and length (L) were 800 and 200 μm, respectively. Finally, 20-nm-thick Al or Ti metal layers were selectively deposited between the source/drain electrodes with dimensions of W/L = 1300/100 μm without subsequent annealing. In the device patterned by photolithography and a lift-off process, the channel W/L and metal layer W/L were 100/50 and 800/35 μm, respectively.

Measurement

Measurements and stability tests to determine the transfer characteristics were conducted using an HP 4156B semiconductor parameter analyzer. The field-effect mobility values were extracted from the saturation region with the drain voltage (V_{DS}) fixed at 10 V. Cross-sectional transmission electron microscopy (TEM) specimens were prepared by in situ lift-out in a dual-beam focused ion beam system (FIB; FEI Helios NanoLabTM). Additionally, X-ray photoelectron spectroscopy (XPS) analyses were performed to study the chemical bonding states of tin cations and oxygen anions using a monochromatic Al Kα X-ray source. Before performing the XPS analyses, the surface of each film was sputtered with a low-energy Ar^+ ion beam (200 eV) for 60 s to eliminate any possible contamination. The peak position was calibrated with respect to the Zn 2p peak, for which the standard binding energy is centered at 1021.7 eV. The threshold voltage (V_{th}) was defined by the gate voltage that induced a drain current of W/L × 10 nA at a V_{DS} of 1 V. Flicker noise measurements were performed using a semiconductor device analyzer (Keysight Technologies B1500A).

Density functional theory (DFT) calculations

All DFT calculations were performed using the Vienna ab initio Simulation Package (VASP)[28,29] with the

projected augmented wave (PAW) potentials[30]. To trace the diffusion of atoms in the interface region between the a-ZBTO and metal Al/Ti layers, first-principles molecular dynamics (MD) calculations were employed. The final structure was then obtained using static DFT calculations. The exchange-correlation functional based on PBEsol (Perdew–Burke–Ernzerhof revised for solids)[31] was used, which is known to describe atomic structures well at a low computational cost. The kinetic energy cutoff for the plane-wave basis set was chosen to be 400 (600) eV for MD calculations (volume optimization). In addition, k-space integration was used with a Γ-point of (1 × 1 × 1) to generate an amorphous structure and with a mesh of (2 × 2 × 2) to optimize the crystal structure. All atomic positions were fully relaxed until the Hellmann–Feynman force on each atom was within 0.01 eV $Å^{-1}$.

To model the interface structure between ZBTO and the metal, the superlattice-like structure used here consisted of a combined a-ZBTO and metal (a-Al/a-Ti) supercell created via the following sequential processes: (i) a-ZBTO (a-metal) based on a (2 × 2 × 8) a-$Z_{1-x}B_x$TO with x = 0.312 supercell of 160 atoms (an a-Al/a-Ti supercell of 64 atoms) was independently generated by first-principles melt-quenching (MQ) MD calculations. Until the total energy converged, MQ-MD calculations for ZBTO (metal) were repeated several times for melting at 4000 (3000) K and quenching at rates from 1.0 K fs^{-1} to 0.5 K fs^{-1} to temperatures from approximately 4000 (3000) K to 10 K. (ii) After the a-ZBTO and a-metal structures were combined, simulation annealing was conducted from 300 K to 50 K (0.2 K fs^{-1}). This process was also repeated until the total energy converged. (iii) To study the diffusion of atoms at the interface while considering the bulk by fixing 43 atoms in the middle region of a-ZBTO, a finite temperature MD simulation was conducted for a long simulation time of 20 ns. The temperature was set at a higher temperature (750 K) than the experimental temperature (approximately room T) to accelerate the atomic diffusion in both the ZBTO and metal layers.

Results and discussion

Effect of the Al metal layer on the ZBTO thin-film layer

Figure 1a, b presents cross-sectional transmission electron microscopy (TEM) images of a-ZBTO films with Ti and Al metal layers, respectively. When a Ti-capping layer is used, the Ti layer is entirely oxidized (Fig. 1a), whereas with the Al-capping layer, a relatively thin oxide (AlO_x) interlayer forms between the Al and a-ZBTO (Fig. 1b). The X-ray photoelectron spectroscopy (XPS) depth

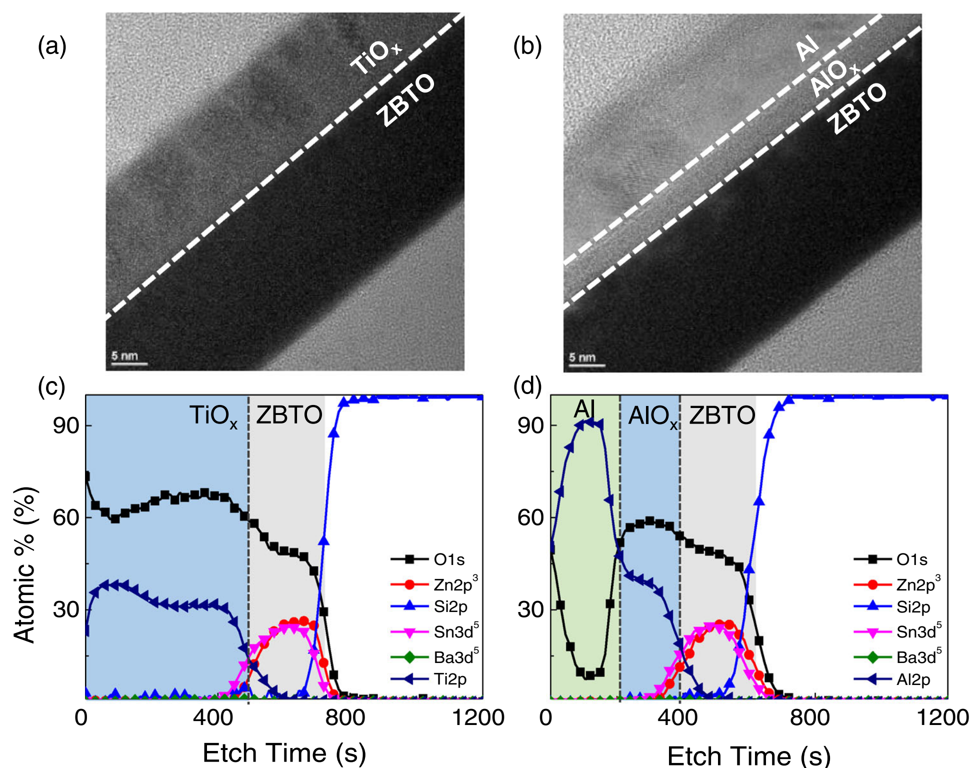

Fig. 1 Formation of oxidized interlayers by metal layers at the interface between metal and ZBTO layers. Cross-sectional TEM images of **a** Ti-capped and **b** Al-capped ZBTO films. XPS depth profile of the ZBTO film with **c** a Ti layer and **d** an Al layer.

profiles of the atomic elements present in the stacked structures in Fig. 1c, d also show that the entire and thin oxidized regions in the Ti and Al metal layers, respectively, are consistent with the aforementioned TEM observations. This difference in oxidation can be easily understood. Because Ti readily oxidizes even upon simple exposure to air[32], the formation of TiO_x on top of a-ZBTO is likely to be spontaneously caused by both oxidation from the ambient environment and consumption of oxygen from the underlying ZBTO. On the other hand, an Al layer is known to form only a very thin and dense oxide on its surface after exposure to air, which prevents further internal oxidation[33]. It is thus reasonable to conclude that the AlO_x interlayer between ZBTO and Al is formed by the consumption of oxygen from the underlying ZBTO.

Figure 2 shows the O 1 s and Sn 3d XPS spectra of the reference ZBTO and metal-assisted ZBTO films. While the spectra from the ZBTO films without a metal layer were collected from the surface of the films, the spectra from the ZBTO films with the metal layer were collected near the metal/semiconductor interface during depth profiling. All the subpeaks are shown in Fig. S1. The O 1 s peaks were resolved into three subpeaks centered at 530.2 (O1), 531.2 (O2), and 532.7 eV (O3). The O1, O2 and O3 peaks represent the signals originating from metal-oxygen bonds, O deficiency, and hydrogen-related bonds, respectively[34]. Figure 2a, b shows that the portions of the O1 and O2 peaks for the reference ZBTO films and ZBTO films with a Ti layer are nearly identical. In contrast, the O2 peak portion increases when an Al metal layer is applied, from 21.5 to 30.3 %, as shown in Fig. 2b. The Gibbs free energies of formation (ΔG_f) of ZnO, SnO_2, BaO, TiO_2 and Al_2O_3 are −318.4, −520.5, −520.4, −889.1, and −1582.3 kJ/mol, respectively[35]. The lowest ΔG_f of Al_2O_3 means that Al has the strongest oxidation power compared to ZnO, SnO_2, BaO, and TiO_2. Therefore, an AlO_x film most likely forms at the Al/ZBTO interface due to the removal of oxygen from the ZBTO layer, which in turn significantly induces O deficiency in the back channel region. On the other hand, the Sn 3d peaks were also resolved into three subpeaks, as shown in Fig. 2c, d. The subpeaks at 487.0, 486.3, and 484.8 eV can be assigned to signals originating from SnO_2 (Sn^{4+}), SnO

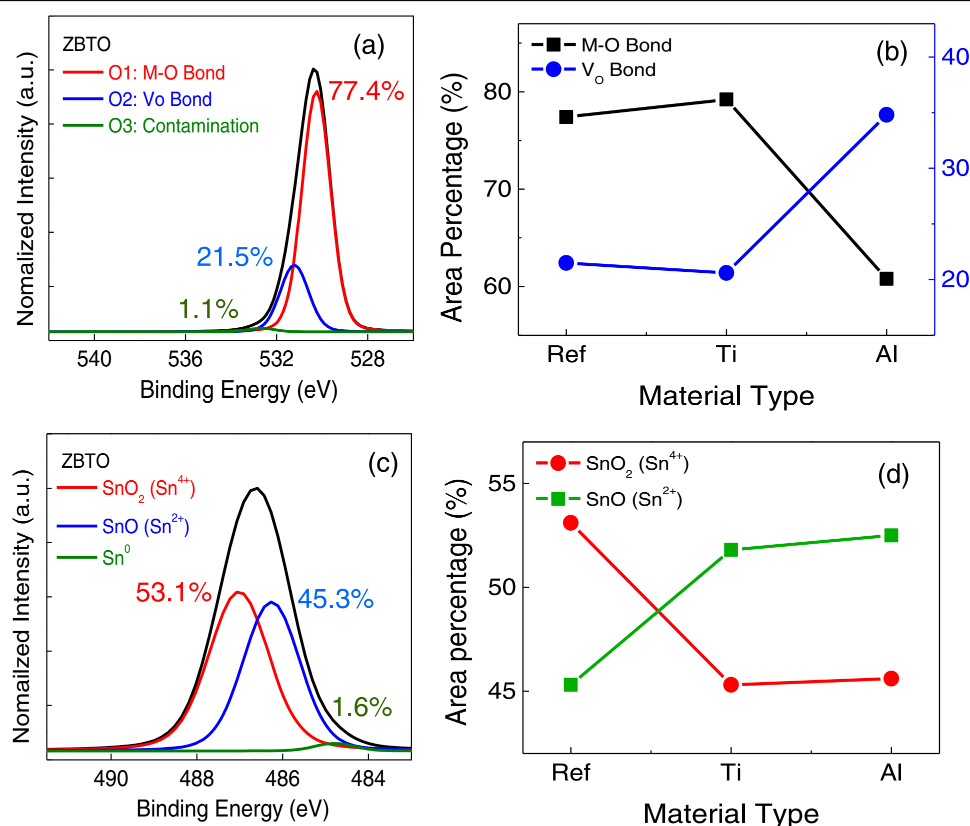

Fig. 2 Chemical bonding state of ZBTO thin-films with metal layers. a XPS O 1 s spectra of the reference ZBTO films. **b** Comparison of the subpeak area percentages for the M-O bond and the V_O bond of the reference and metal-assisted ZBTO films from the O 1 s spectra. **c** XPS Sn $3d_{5/2}$ spectra of the reference ZBTO films. **d** Comparison of the subpeak area percentages for SnO_2 and SnO of the reference and metal-assisted ZBTO films from the Sn $3d_{5/2}$ spectra.

Table 1 Hall effect measurement results of the reference and Al-capped ZBTO thin-films.

TFT	Bulk concentration	Sheet resistance
ZBTO	−7.87 E + 15	104 MΩ/□
ZBTO – with Al layer	−1.91 E + 16	5.2 MΩ/□

(Sn^{2+}), and metallic Sn (Sn^0) bonds[36]. The increased portions of the Sn^{2+} subpeak in the ZBTO films with the metal layer suggest that the transition of SnO_2 to SnO ($Sn^{4+} + 2e^- \rightarrow Sn^{2+}$) may occur due to the electrons injected from the metal layer. Because the work functions of Al and Ti are similar at 4.28 and 4.33 eV[37], respectively, the effects of the electron injection by the two metal layers would be nearly identical. This could be confirmed by the result that the increase degrees of Sn^{2+}-related subpeaks in both films with the metal layers are nearly identical.

Note that the oxygen and tin subpeak portions in the bulk regions, as shown in Supplementary Fig. S2, are nearly identical regardless of the presence or absence of a metal layer. The above results indicate that the a-ZBTO channel with an Al metal layer consists of two regions, a conductive region on top with a relatively high concentration of free carriers induced by the O deficiency (n^+ layer) and a relatively unaltered ZBTO bulk region (n layer) on the bottom, which can itself form a metal-induced n^+/n homojunction within the semiconductor layer.

Furthermore, the Hall effect measurement results showed that the carrier concentration of ZBTO thin-films was increased approximately 2 times by the Al metal layer, as listed in Table 1. This result clearly confirms the effect of the Al metal layer on the ZBTO thin-films. Additionally, the increased carrier concentration due to the Al metal layer (~$10^{16}/cm^3$) is not sufficient to form a degenerate channel, which is reported to occur through the injection of a large number of free-electron carriers[38]. Therefore, a degenerate channel would not be formed in the ZBTO channel.

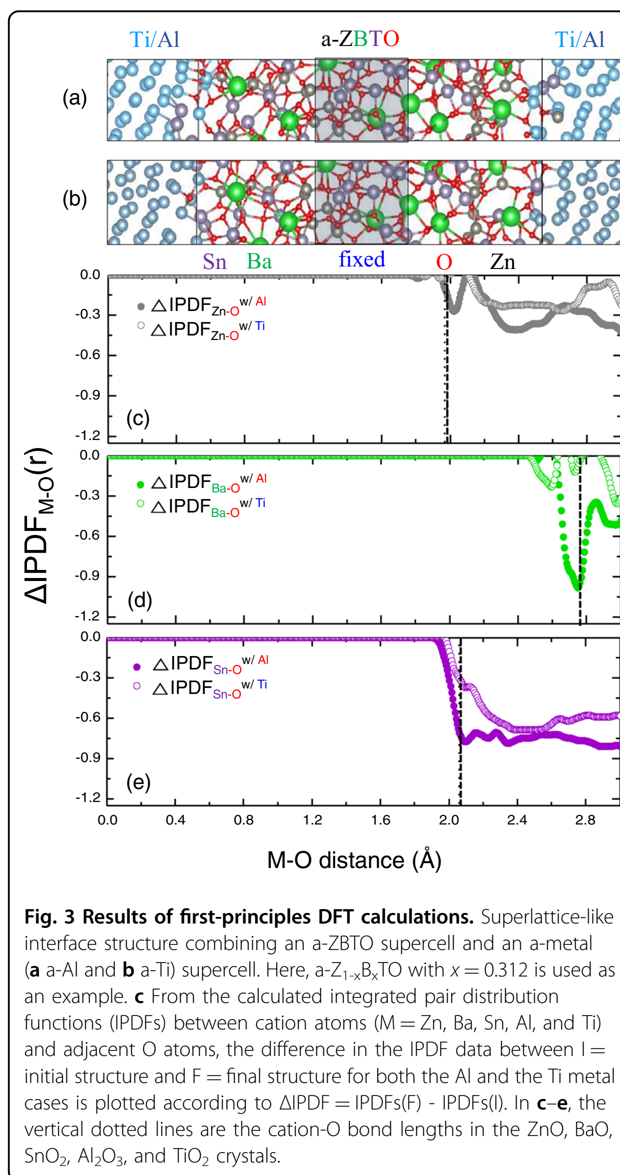

Fig. 3 Results of first-principles DFT calculations. Superlattice-like interface structure combining an a-ZBTO supercell and an a-metal (**a** a-Al and **b** a-Ti) supercell. Here, a-$Z_{1-x}B_xTO$ with $x = 0.312$ is used as an example. **c** From the calculated integrated pair distribution functions (IPDFs) between cation atoms (M = Zn, Ba, Sn, Al, and Ti) and adjacent O atoms, the difference in the IPDF data between I = initial structure and F = final structure for both the Al and the Ti metal cases is plotted according to ΔIPDF = IPDFs(F) - IPDFs(I). In **c**–**e**, the vertical dotted lines are the cation-O bond lengths in the ZnO, BaO, SnO_2, Al_2O_3, and TiO_2 crystals.

First-principles DFT calculations

Although shown in the XPS analysis above, it is fundamental to theoretically verify whether, among Al and Ti, the Al metal layer better removes oxygen atoms from the back channel at the interface between a-ZBTO and the metal-capping layer. To do this, first-principles DFT calculations were applied to study the interface of a-ZBTO with a metal-capping layer. Here, the interface structure was modeled by a superlattice-like structure in which a (2 × 2 × 8) ZBTO supercell of 160 atoms and a metal (Al or Ti) supercell of 64 atoms were combined (see Fig. 3a, b). For comparison of the intermixing of atoms for the two cases of Al and Ti, a finite-temperature molecular dynamics (MD) simulation was conducted with a long simulation time of 20 ns at a temperature of 750 K, which is higher than the experimental temperature, to accelerate the atomic diffusion in the ZBTO-metal structure (see the DFT section of Experimental Methods). Based on the initial (I) and final (F) structures before and after the finite-temperature MD simulation, the relative trends for the Al and Ti metals were compared by analyzing the integrated pair distribution function (*IPDF*) data before and after the finite-temperature MD simulation. Figure 3c–e shows the differences (*ΔIPDFs*) in the average data per atom for the IPDF between cations (Zn, Ba, Sn and metals such as Al and Ti) and O for the two cases calculated according to *ΔIPDF = IPDF(F) - IPDF(I)*. Interestingly, the coordination numbers for all of the Zn, Ba, and Sn cations with O atoms were calculated and found to

be significantly reduced more by the Al metal-capping layer than by the Ti metal-capping layer, depending on the type of cation, similar to the experimental XPS results. In particular, the *ΔIPDFs* vary slightly between the Al and Ti cases for Zn and Sn but dramatically for Ba (Fig. 3c–e). This means that the highly O-deficient n^+ layer at the interface of the Al-ZBTO back channel forms because the Al atoms strongly pull the O atoms from the ZBTO layer to the Al metal layer. The superiority of the Al metal can be easily understood to be due to the greater heat of formation of Al_2O_3 than that of TiO_2. Therefore, the role of the metal-capping layer in the formation of the O-deficient region of the a-ZBTO channel is well characterized in terms of the diffusion of atoms during the production of the experimental TFT device.

Electrical characteristics of the thin-film transistors

Figure 4a, b shows the device structure and an optical micrograph of the ZBTO TFTs with a metal layer. The metal layer was deposited onto the ZBTO film at half the length of the channel between the source and drain electrodes. The transfer curves of TFT devices based on the reference and metal-assisted ZBTO are shown in Fig. 4c–e, and the extracted transfer parameters are listed in Table 2. The extracted saturation mobility values with respect to the gate voltage are shown in Fig. 4f. As anticipated, the application of a Ti metal layer results in an increase in the field-effect mobility by approximately twofold (~53.7 cm^2/Vs). This improved mobility of Ti-assisted TFTs originates from the electrons injected from the metal layer, as confirmed by the increase in the Sn^{2+}-related peak in the Sn3d XPS spectra of both metal-assisted ZBTO films. Unlike the Ti capping case, which corresponds to the typical field-effect mobility increase due to the metal-capping method, a further enhancement is observed in the presence of an Al capping layer with a remarkable peak mobility outcome of 153.4 cm^2/Vs. This indicates that in addition to the electron injection effect, the main cause of the significantly improved mobility of the Al-assisted TFTs is the increase in the effective carriers stemming from the highly conductive n^+ layer formed within the ZBTO layer.

For comparison, other conventional oxide semiconductor materials were evaluated using an Al metal layer. Figure 5a depicts a schematic diagram of the electron injection mechanism from the conduction region to the bulk region in the active layer. Generally, conventional oxide semiconductors, such as IZO and ZTO, contain numerous oxygen-related and disorder defects that act as electron scattering/trapping centers[39]. Therefore, for conventional oxide semiconductors, most of the injected electrons from the n^+ layer could be trapped by various defects in the n layer (front channel layer), thereby limiting the mobility improvement effect. In contrast, for ZBTO, oxygen-related and disorder defects are effectively reduced by the incorporation of BTO[27]. It has been reported that incorporation of BTO significantly decreases the band tail states or oxygen-related defects. As a result of the decreased defect density in ZBTO, most of the generated or injected electrons from the n^+ layer can be transported without serious scattering/trapping[27]. Therefore, an ultrahigh field-effect mobility can be achieved when using ZBTO as an active layer. Figure 5b indeed indicates a lower mobility improvement due to the Al metal layer for the conventional oxide IZO and ZTO TFTs compared to the ZBTO TFTs. Individual transfer curves of metal-assisted conventional oxide TFTs are shown in Supplementary Fig. S3, and the extracted transfer parameters are listed in Supplementary Table S1. For comparison, Fig. 5c shows the field-effect mobility outcomes of all TFTs.

Low-frequency noise (LFN) characterization of the thin-film transistors

To probe the prevailing carrier transport mechanisms, we measured the 1/f noise of the ZBTO and Al-assisted ZBTO TFTs at $V_{DS} = 1.0$ V and plotted the current noise spectral densities (S_{ID}) versus the frequency, as seen in the inset of Fig. 6a. The slopes for both devices under all bias conditions obey the typical 1/f noise theory[40]. Figure 6a shows the normalized current noise spectral density (S_{ID}/I_D^2) as a function of $|V_{GS} - V_{TH}|$ at 80 Hz. The slope value of −1.5 for the ZBTO TFTs indicates that the electrons are scattered by coherent trap sites composed of bulk traps and interface traps, as illustrated in Fig. 6c. In contrast, the slope value of almost −2 for the Al-assisted ZBTO TFTs indicates that the electrons are scattered mainly by interface traps, as depicted in Fig. 6d[40–44]. As a result of the reduced bulk trap sites, the Al-assisted ZBTO TFTs show fairly outstanding transfer characteristics compared to the ZBTO TFTs. The improved charge transport may originate from the excess electrons induced by the Al metal layer, which could passivate the bulk defect states in the ZBTO channel through the Al assisting layer. For further confirmation of transport mechanisms, the slopes of input-referred noise (S_{VG}) were compared (see Fig. 6b).

$$S_{VG} = S_{VFB}\left[1 + \alpha\mu_{eff}C_{ox}(V_{GS} - V_{TH})\right]^2 \quad (1)$$

Here, S_{VFB} is the flat-band voltage noise density, α is the Coulomb scattering coefficient, μ_{eff} is the effective mobility, and C_{ox} is the dielectric capacitance per unit area. The slope of the ZBTO TFTs shows a tendency similar to that

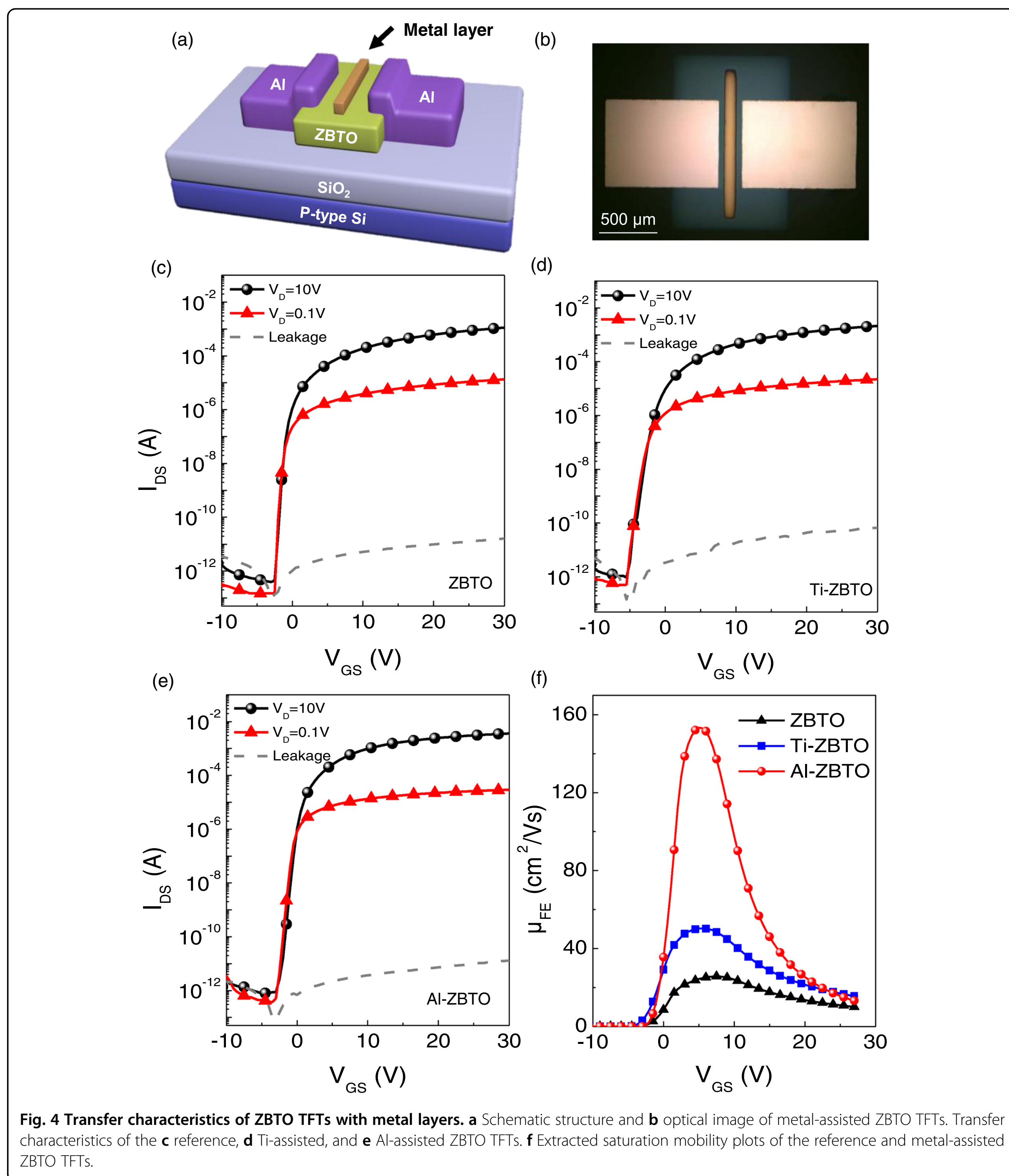

Fig. 4 Transfer characteristics of ZBTO TFTs with metal layers. a Schematic structure and **b** optical image of metal-assisted ZBTO TFTs. Transfer characteristics of the **c** reference, **d** Ti-assisted, and **e** Al-assisted ZBTO TFTs. **f** Extracted saturation mobility plots of the reference and metal-assisted ZBTO TFTs.

in Eq. (1), suggesting that the carrier transport is influenced by the mechanism of bulk trap scattering[42].

$$S_{VG} = \frac{q^2 \cdot \mathrm{k} \cdot \mathrm{T} \cdot \mathrm{N}_T}{\mathrm{C}_{ox}^2 \cdot W \cdot L \cdot \gamma \cdot f} \quad (2)$$

In this equation, q is the electronic charge; kT is the thermal energy; N_T is the oxide trap density; W and L are the channel width and length, respectively; γ is the attenuation coefficient; and f is the frequency[45]. In contrast, the slope of the Al-assisted TFTs is zero, coinciding with Eq. (2), which corresponds to the interface-trap-dominant model.

Reliabilities of the thin-film transistors

Figure 7a shows the device reliability test results for the reference and metal-assisted ZBTO TFTs under negative bias stress (NBS) and positive bias stress (PBS) conducted with a fixed gate voltage $V_{GS} = \pm 20$ V and a drain voltage $V_{DS} = 0.1$ V for 3600 s. Additionally, the amounts of threshold voltage shift under NBS and PBS are listed in Table 3. Refer to the detailed transfer curves of ZBTO TFTs and metal-assisted ZBTO TFTs in Fig. S4. The threshold voltage shifts during the bias stress test generally depend on the amount of trapped charge in the front channel region near the semiconductor/gate dielectric interface[46,47]. Despite the conductive region induced in the back channel due to the formation of the AlO_x interlayer, the metal-assisted ZBTO TFTs exhibit relatively stable behavior, comparable to the reference devices. This suggests that the front channel is relatively less affected by the presence of the metal layer, as predicted from the aforementioned thin-film characterization results (e.g., XPS).

Table 2 Extracted transfer parameters of the reference, Ti-assisted, and Al-assisted ZBTO TFTs.

ZBTO TFT	μ_{FE} (cm^2/Vs)	S.S. (V/dec)	V_{th} (V)	I_{on}/I_{off}
reference	20.8 ± 2.70	0.32 ± 0.06	−0.05 ± 0.29	~10^9
with Ti layer	53.7 ± 8.60	0.44 ± 0.08	−1.85 ± 0.42	~10^9
with Al layer	153 ± 16.6	0.37 ± 0.07	−0.77 ± 0.35	~10^9

The long-term stability of the Al-assisted ZBTO TFTs was evaluated, as shown in Fig. 7b. Figure 7c shows the extracted transfer parameters as a function of the air exposure time. The electrical characteristics are well preserved over a period of 90 days under ambient air. The device performance enhanced by the application of the metal layer does not significantly degrade, which suggests that stable operation of the TFTs is possible with good long-term operational reliability.

For application to high-resolution displays and highly integrated circuits, the corresponding TFT size should be reduced. Accordingly, the possibility of downscaling the Al-assisted ZBTO TFTs using photolithography and a lift-off process was investigated. The channel layer width/length of the downscaled (DS) device was reduced from 800/200 to 100/50 µm. Supplementary Fig. S5 exhibits the transfer curves of DS-ZBTO TFTs with and without an Al

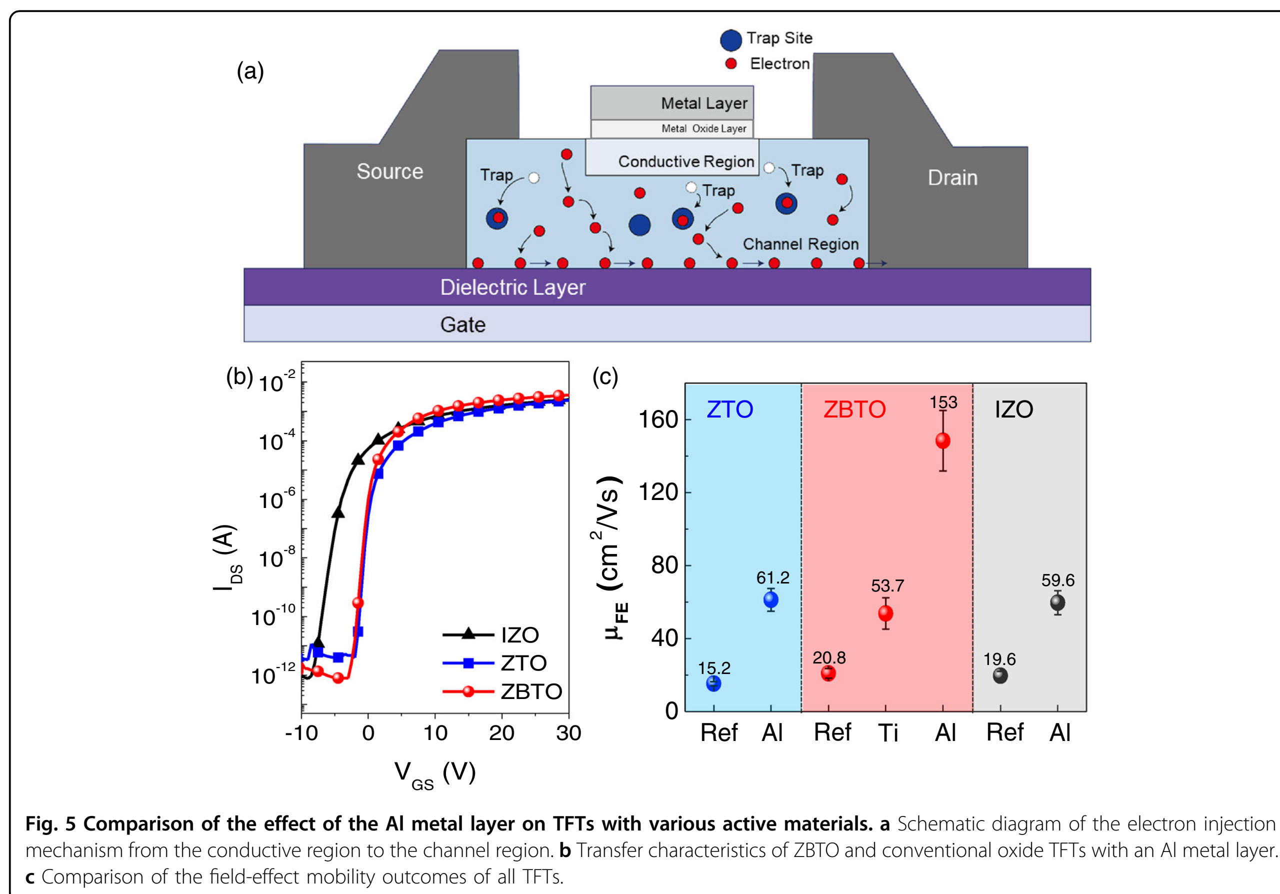

Fig. 5 Comparison of the effect of the Al metal layer on TFTs with various active materials. a Schematic diagram of the electron injection mechanism from the conductive region to the channel region. **b** Transfer characteristics of ZBTO and conventional oxide TFTs with an Al metal layer. **c** Comparison of the field-effect mobility outcomes of all TFTs.

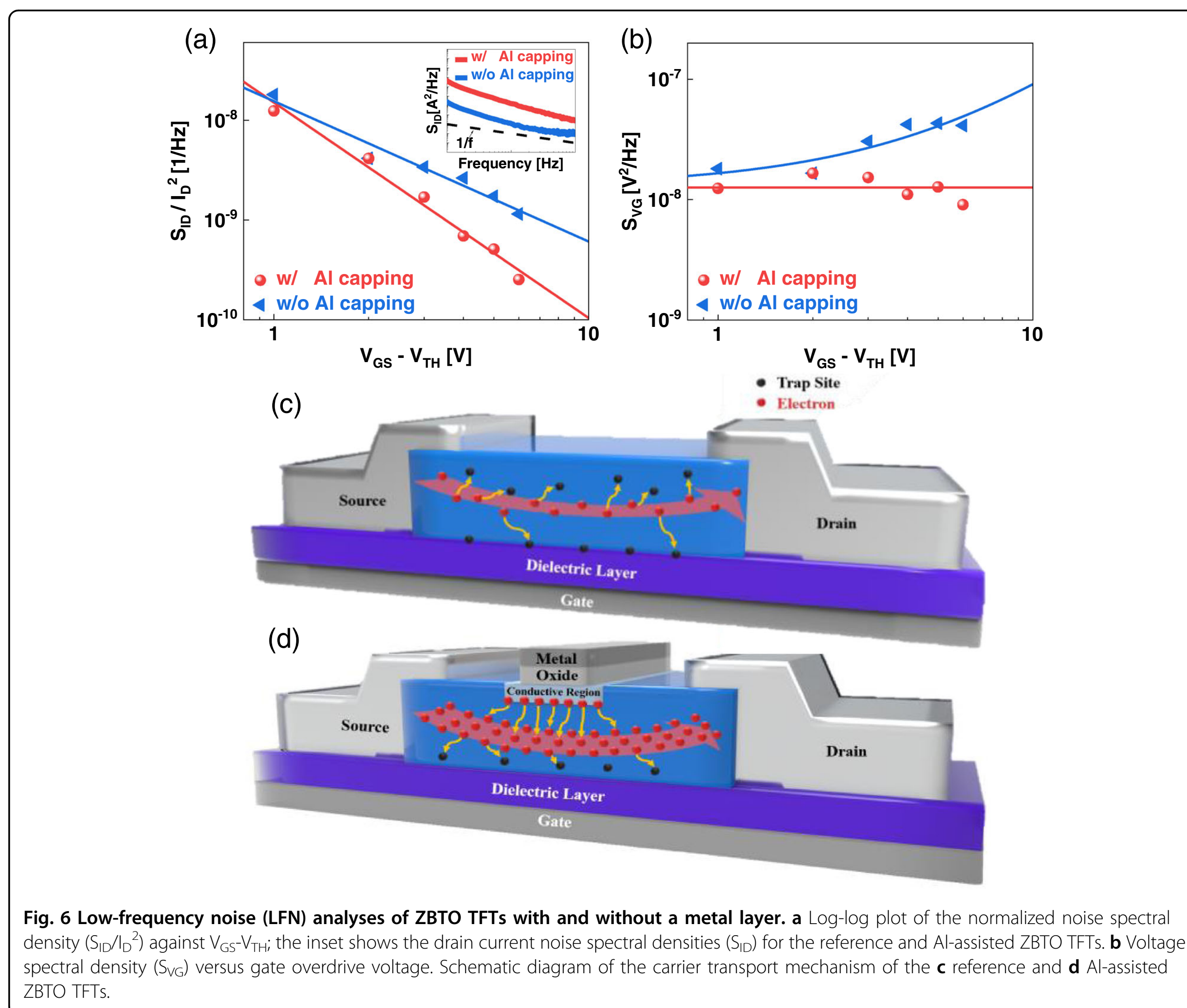

Fig. 6 Low-frequency noise (LFN) analyses of ZBTO TFTs with and without a metal layer. **a** Log-log plot of the normalized noise spectral density (S_{ID}/I_D^2) against V_{GS}-V_{TH}; the inset shows the drain current noise spectral densities (S_{ID}) for the reference and Al-assisted ZBTO TFTs. **b** Voltage spectral density (S_{VG}) versus gate overdrive voltage. Schematic diagram of the carrier transport mechanism of the **c** reference and **d** Al-assisted ZBTO TFTs.

metal layer. It was found that the field-effect mobility of the Al-assisted DS-ZBTO TFTs was improved to more than ~120 cm^2/Vs without large changes in the other transfer parameters. Although TFT fabrication by the lithography process requires further optimization, such as of the area ratio of the metal layer to the channel, the aforementioned effect of an improved mobility due to the metal layer was clearly confirmed for TFTs with a small feature size.

Finally, the extracted field-effect mobility and channel length (device scale) in previously reported works and this work are depicted in Fig. 8. Compared to other works, this work represents remarkably improved mobility (~153 cm^2/Vs) without a stabilization or postannealing process. Moreover, most of the previous reports that adopted the metal capping process for enhancing the field-effect mobility were limited to TFTs with relatively long channel lengths. In the case of scaled-down TFTs, only a few papers have reported the metal capping process, with relatively low field-effect mobilities (>50 cm^2/Vs). However, our work shows greatly enhanced field-effect mobility (~120 cm^2/Vs) even for scaled-down TFTs (L = 50 μm). Consequently, we suggest that high-performance a-ZBTO TFTs with Al capping layers could be good candidates for future high-resolution display applications.

Conclusions

In summary, we investigated the effects of metal-capping layers on ZBTO films and the associated thin-film device characteristics. The application of a highly oxidizing metal, such as Al, to ZBTO results in the creation of an AlO_x interlayer, accompanied by the formation of an oxygen-deficient interfacial (n^+) layer in the n-channel ZBTO film underneath, leading to an n^+/n homojunction structure. This results in only an increase in the free carrier concentration in the front ZBTO

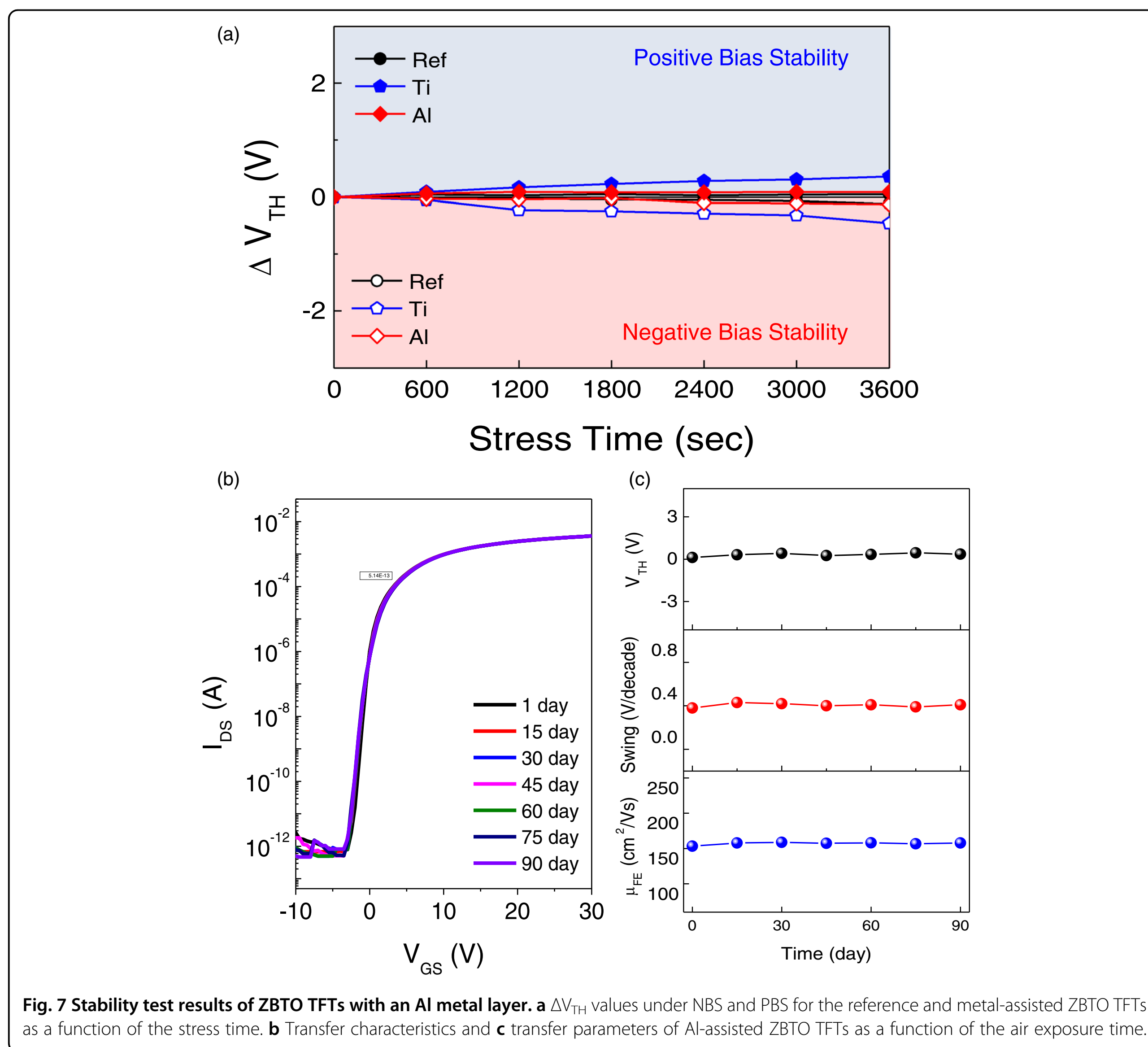

Fig. 7 Stability test results of ZBTO TFTs with an Al metal layer. a ΔV_{TH} values under NBS and PBS for the reference and metal-assisted ZBTO TFTs as a function of the stress time. **b** Transfer characteristics and **c** transfer parameters of Al-assisted ZBTO TFTs as a function of the air exposure time.

Table 3 ΔV_{TH} values of the reference, Ti-assisted, and Al-assisted ZBTO TFTs after NBS and PBS tests.

NBS			
TFT	ZBTO	ZBTO with Ti layer	ZBTO with Al layer
ΔV_{th} (V)	−0.12	−0.46	−0.13
PBS			
TFT	ZBTO	ZBTO with Ti layer	ZBTO with Al layer
ΔV_{th} (V)	0.05	0.36	0.09

channel layer with sufficiently limited scattering centers, remarkably enhancing the field-effect mobility of the corresponding TFTs. In addition, first-principles DFT calculations were utilized to determine the oxidation tendency of Al_2O_3 relative to that of TiO_2, which is the driving force behind the formation of the highly conductive n^+ layer in the ZBTO layer. As a result, the Al-assisted ZBTO TFTs achieved a noticeably enhanced field-effect mobility of 153.4 cm^2/Vs, far superior to those of other Al-assisted conventional oxide TFTs. From 1/f noise measurements and characterization of ZBTO and Al-assisted ZBTO TFTs, we found that the carrier transport of ZBTO TFTs with the Al assisting layer is enhanced due to the reduced bulk trap sites. The effect of the mobility improvement was also confirmed in small-sized ZBTO TFTs with an Al layer fabricated by lithography. Moreover, reliability tests indicate that the front channel of the metal-assisted devices is relatively less affected. These results suggest that the formation of a metal-induced oxide n^+/n homojunction for ultrahigh

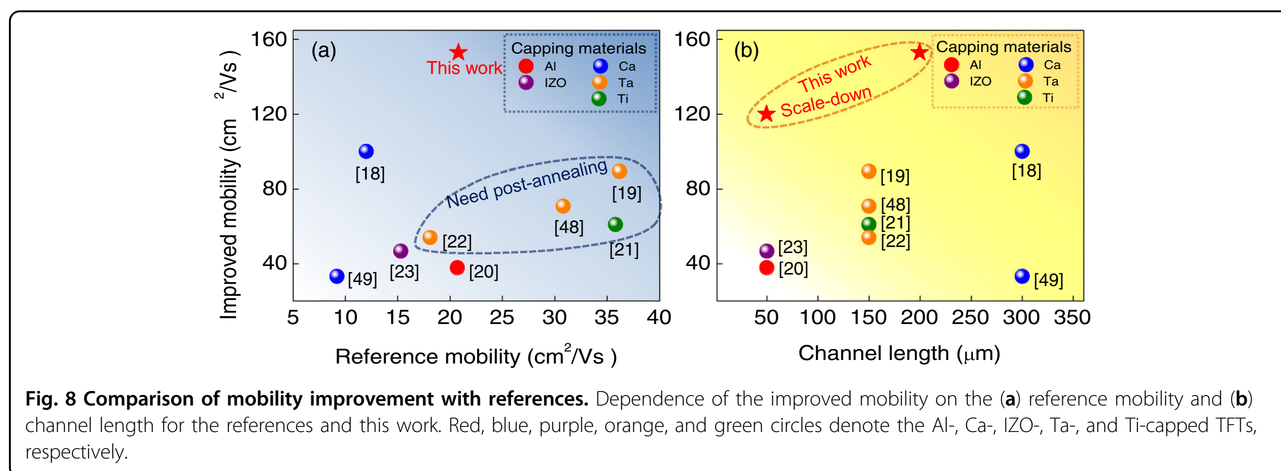

Fig. 8 Comparison of mobility improvement with references. Dependence of the improved mobility on the (**a**) reference mobility and (**b**) channel length for the references and this work. Red, blue, purple, orange, and green circles denote the Al-, Ca-, IZO-, Ta-, and Ti-capped TFTs, respectively.

electron mobility transistors could be a cost-effective and useful route to replace current low-temperature poly-Si (LTPS) TFT technology.

Acknowledgements

This work was supported by the Basic Science Research Program through the National Research Foundation of Korea (NRF) funded by the Ministry of Education (Grant No: NRF-2019R1I1A2A01064153), by the National Institute of Supercomputing and Network/Korea Institute of Science and Technology support (Grant KSC-2018-CRE-0095), and by the MOTIE (Ministry of Trade, Industry & Energy (Grant No: 10051403)) and KDRC (Korea Display Research Corporation) support program for the development of future device technology for the display industry. Work at KAIST was also supported by the NRF (2018R1D1A1B07048465), NRF (2018R1A2A2A14079326), and SRC (2016R1A5A1008184). Additionally, this work was supported by the BK21 plus program through the National Research Foundation (NRF) funded by the Ministry of Education of Korea.

Author details

[1]Department of Materials Science and Engineering, Chungnam National University, Daejeon 34134, Republic of Korea. [2]School of Electrical Engineering, Korea Advanced Institute of Science and Technology (KAIST), 291, Daehak-ro, Yuseong-gu, Daejeon, Republic of Korea. [3]Semiconductor Process Laboratory, WONIK IPS, Gyeonggi-do 17709, Republic of Korea. [4]National Nano Fab Center, Daejeon 305-806, Republic of Korea. [5]Graduate School of Nanoscience and Technology and Department of Physics, Korea Advanced Institute of Science and Technology, Daejeon 34141, Republic of Korea

Conflict of interest

The authors declare that they have no conflict of interest.

Publisher's note

Springer Nature remains neutral with regard to jurisdictional claims in published maps and institutional affiliations.

Supplementary information is available for this paper at https://doi.org/10.1038/s41427-020-00271-y.

Received: 28 April 2020 Revised: 22 October 2020 Accepted: 17 November 2020.
Published online: 18 December 2020

References

1. Nomura, K. et al. Room-temperature fabrication of transparent flexible thin-film transistors using amorphous oxide semiconductors. *Nature* **432**, 488–492 (2004).
2. Hoffman, R. L., Norris, B. J. & Wager, J. F. ZnO-based transparent thin-film transistors. *Appl. Phys. Lett.* **82**, 733–735 (2003).
3. Jeong, J. K. The status and perspectives of metal oxide thin-film transistors for active matrix flexible displays. *Semicond. Sci. Technol.* **26**, 034008 (2011).
4. Lee, H. N. et al. Oxide TFT with multilayer gate insulator for backplane of AMOLED device. *J. Soc. Inf. Disp.* **16**, 265–272 (2008).
5. Kamiya, T., Nomura, K. & Hosono, H. Present status of amorphous In–Ga–Zn–O thin-film transistors. *Sci. Technol. Adv. Mater.* **11**, 044305 (2010).
6. Lee, S., Bierig, B. & Paine, D. C. Amorphous structure and electrical performance of low-temperature annealed amorphous indium zinc oxide transparent thin film transistors. *Thin Solid Films* **520**, 3764–3768 (2012).
7. Barquinha, P., Goncalves, G., Pereira, L., Martins, R. & Fortunato, E. Effect of annealing temperature on the properties of IZO films and IZO based transparent TFTs. *Thin Solid Films* **515**, 8450–8454 (2007).
8. Seo, J. S. & Bae, B. S. Improved electrical performance and bias stability of solution-processed active bilayer structure of indium zinc oxide based TFT. *ACS Appl. Mater. Interfaces* **6**, 15335–15343 (2014).
9. Tomai, S. et al. High-performance thin film transistor with amorphous In2O3–SnO2–ZnO channel layer. *Jpn. J. Appl. Phys.* **51**, 03CB01 (2012).
10. Sheng, J., Han, J. H., Choi, W. H., Park, J. & Park, J. S. Performance and stability enhancement of In–Sn–Zn–O TFTs using SiO2 gate dielectrics grown by low temperature atomic layer deposition. *ACS Appl. Mater. Interfaces* **9**, 42928–42934 (2017).
11. Zhao, Y. et al. High-performance transistors based on zinc tin oxides by single spin-coating process. *Langmuir* **29**, 151–157 (2013).
12. Chiang, H. Q., Wager, J. F., Hoffman, R. L., Jeong, J. & Keszler, D. A. High mobility transparent thin-film transistors with amorphous zinc tin oxide channel layer. *Appl. Phys. Lett.* **86**, 013503 (2005).
13. Ryu, M. et al. High mobility zinc oxynitride-TFT with operation stability under light-illuminated bias-stress conditions for large area and high resolution display applications. In 2012 International Electron Devices Meeting. IEEE. pp. 5–6 (2012).
14. Ok, K. C., Jeong, H. J., Kim, H. S. & Park, J. S. Highly stable ZnON thin-film transistors with high field-effect mobility exceeding 50cm2/Vs. *IEEE Electron Device Lett.* **36**, 38–40 (2014).
15. Kim, H. D. et al. Effects of fluorine doping on the electrical performance of ZnON thin-film transistors. *ACS Appl. Mater. Interfaces* **9**, 24688–24695 (2017).
16. Park, J. S. et al. High performance and stability of double-gate Hf–In–Zn–O thin-film transistors under illumination. *IEEE Electron Device Lett.* **31**, 960–962 (2010).
17. Son, K. S. et al. Characteristics of double-gate Ga–In–Zn–O thin-film transistor. *IEEE Electron Device Lett.* **31**, 219–221 (2010).
18. Zan, H. W., Yeh, C. C., Meng, H. F., Tsai, C. C. & Chen, L. H. Achieving high field-effect mobility in amorphous indium-gallium-zinc oxide by capping a strong reduction layer. *Adv. Mater.* **24**, 3509–3514 (2012).
19. Kim, T., Kim, M. J., Lee, J. & Jeong, J. K. Boosting carrier mobility in zinc oxynitride thin-film transistors via tantalum oxide encapsulation. *ACS Appl. Mater. Interfaces* **11**, 22501–22509 (2019).

20. Lee, B. H., Sohn, A., Kim, S. & Lee, S. Y. Mechanism of carrier controllability with metal capping layer on amorphous oxide SiZnSnO semiconductor. *Sci. Rep.* **9**, 1–7 (2019).
21. Ji, H. et al. Improvement in field-effect mobility of indium zinc oxide transistor by titanium metal reaction method. *IEEE Trans. Electron Devices* **62**, 1195–1199 (2015).
22. Shin, Y. et al. The mobility enhancement of indium gallium zinc oxide transistors via low-temperature crystallization using a tantalum catalytic layer. *Sci. Rep.* **7**, 1–10 (2017).
23. Kim, K. T., Kim, J., Kim, Y. H. & Park, S. K. In-situ metallic oxide capping for high mobility solution-processed metal-oxide TFTs. *IEEE Electron Device let.* **35**, 850–852 (2014).
24. Kamiya, T., Nomura, K. & Hosono, H. Origin of definite Hall voltage and positive slope in mobility-donor density relation in disordered oxide semiconductors. *Appl. Phys. Lett.* **96**, 122103 (2010).
25. Germs, W. C. Charge transport in amorphous InGaZnO thin-film transistors. *Phys. Rev. B* **86**, 155319 (2012).
26. Fishchuk, I. I. et al. Interplay between hopping and band transport in high-mobility disordered semiconductors at large carrier concentrations: The case of the amorphous oxide InGaZnO. *Phys. Rev. B.* **93**, 195204 (2016).
27. Nahm, H. H., Kim, H. D., Park, J. M., Kim, H. S. & Kim, Y. H. Amorphous mixture of two indium-free BaSnO3 and ZnSnO3 for thin-film transistor with balanced performance and stability. *ACS Appl. Mater. Interfaces* **12**, 3719–3726 (2019).
28. Kresse, G. & Furthmüller, J. Self-interaction correction to density functional approximation for many electron systems. *Phys. Rev. B.* **54**, 11169 (1996).
29. Kresse, G. & Furthmüller, J. Efficiency of ab-initio total energy calculations for metals and semiconductors using a plane-wave basis set. *Comput. Mater. Sci.* **6**, 15–50 (1996).
30. Blöchl, P. E. Projector augmented-wave method. *Phys. Rev. B* **50**, 17953 (1994).
31. Perdew, J. P. et al. Restoring the density-gradient expansion for exchange in solids and surfaces. *Phys. Rev. Lett.* **100**, 136406 (2008).
32. Feng, B. et al. Surface characterization of titanium and adsorption of bovine serum albumin. *Mater. Charact.* **49**, 129–137 (2002).
33. Hasnaoui, A. et al. Molecular dynamics simulations of the nano-scale room-temperature oxidation of aluminum single crystals. *Surf. Sci.* **579**, 47–57 (2005).
34. Wang, Y. H. et al. Performance improvement of atomic layer-deposited ZnO/Al 2 O 3 thin-film transistors by low-temperature annealing in air. *IEEE Trans. Electron Devices* **63**, 1893–1898 (2016).
35. James, S. in Lange's handbook of Chemistry, pps 6-1 to 6-147 (McGraw-Hill Education LLC, USA, 2005).
36. Han, S. J. et al. Composition-dependent structural and electrical properties of p-type SnOx thin films prepared by reactive DC magnetron sputtering: Effects of oxygen pressure and heat treatment. *RSC Adv.* **6**, 71757–71766 (2016).
37. Lide, D. R. in CRC Handbook of Chemistry and Physics 77th ed. pp. 12 (CRC press, Boca Raton, New York, 1996).
38. Chen, C. et al. Analysis of ultrahigh apparent mobility in oxide field-effect transistors. *Adv. Sci.* **6**, 1801189 (2019).
39. Kim, G. H. et al. Investigation of the effects of Mg incorporation into InZnO for high-performance and high-stability solution-processed thin film transistors. *Appl. Phys. Lett.* **96**, 163506 (2010).
40. Yun, S. J., Lee, K. H., Skarp, J., Kim, H. R. & Nam, K. S. Dependence of atomic layer-deposited Al2O3 films characteristics on growth temperature and Al precursors of Al (CH3)3 and AlCl3. *J. Vac. Sci. Technol. A.* **15**, 2993–2997 (1997).
41. Cho, I. T. et al. Comparative study of the low-frequency-noise behaviors in a-IGZO thin-film transistors with Al2O3 and Al2O3/SiNx gate dielectrics. *IEEE Electron Device Lett.* **30**, 828–830 (2009).
42. Jeon, S. et al. Low-frequency noise performance of a bilayer InZnO–InGaZnO thin-film transistor for analog device applications. *IEEE Electron Device Lett.* **31**, 1128–1130 (2010).
43. Choi, H. S. et al. The impact of active layer thickness on low-frequency noise characteristics in InZnO thin-film transistors with high mobility. *Appl. Phys. Lett.* **100**, 173501 (2012).
44. Kim, T., Nam, Y., Hur, J., Park, S. H. K. & Jeon, S. The influence of hydrogen on defects of In–Ga–Zn–O semiconductor thin-film transistors with atomic-layer deposition of Al 2 O 3. *IEEE Electron Device Lett.* **37**, 1131–1134 (2016).
45. Choi, H. S. et al. Verification of interface state properties of a-InGaZnO thin-film transistors with SiNx and SiO2 gate dielectrics by low-frequency noise measurements. *IEEE Electron Device Lett.* **32**, 1083–1085 (2011).
46. Cross, R. B. M. & De Souza, M. M. Investigating the stability of zinc oxide thin film transistors. *Appl. Phys. Lett.* **89**, 263513 (2006).
47. Suresh, A. & Muth, J. F. Bias stress stability of indium gallium zinc oxide channel based transparent thin film transistors. *Appl. Phys. Lett.* **92**, 033502 (2008).
48. Kim, S. T. et al. Achieving high carrier mobility exceeding 70 cm 2/Vs in amorphous zinc tin oxide thin-film transistors. *Electron. Mater. Lett.* **13**, 406–411 (2017).
49. Zan, H.-W. et al. Dual gate indium-gallium-zinc-oxide thin film transistor with an unisolated floating metal gate for threshold voltage modulation and mobility enhancement. *Appl. Phys. Lett.* **98**, 153506 (2011).